The Astrophysical Journal Letters, 936:L5 (9pp), 2022 September 1 https://doi.org/10.3847/2041-8213/ac7bed

Bridging the Bondi and Event Horizon Scales: 3D GRMHD Simulations Reveal X-shaped Radio Galaxy Morphology

Aretaios Lalakos[1], Ore Gottlieb[1], Nicholas Kaaz[1], Koushik Chatterjee[2], Matthew Liska[3], Ian M. Christie, Alexander Tchekhovskoy[1], Irina Zhuravleva[4], and Elena Nokhrina[5]
[1] Center for Interdisciplinary Exploration & Research in Astrophysics (CIERA), Physics & Astronomy, Northwestern University, Evanston, IL 60202, USA
lalakos@u.northwestern.edu
[2] Black Hole Initiative at Harvard University, 20 Garden Street, Cambridge, MA 02138, USA
[3] John Harvard Distinguished Science and ITC Fellow; Institute for Theory and Computation, Harvard University, 60 Garden Street, Cambridge, MA 02138, USA
[4] Department of Astronomy and Astrophysics, The University of Chicago, Chicago, IL 60637, USA
[5] Moscow Institute of Physics and Technology, Dolgoprudny, Institutsky per., 9, Moscow region, 141700, Russia
Received 2022 February 23; revised 2022 June 16; accepted 2022 June 24; published 2022 August 29

Abstract

X-shaped radio galaxies (XRGs) produce misaligned X-shaped jet pairs and make up $\lesssim$10% of radio galaxies. XRGs are thought to emerge in galaxies featuring a binary supermassive black hole (SMBH), SMBH merger, or large-scale ambient medium asymmetry. We demonstrate that XRG morphology can naturally form without such special, preexisting conditions. Our 3D general-relativistic magnetohydrodynamic (GRMHD) simulation for the first time follows magnetized rotating gas from outside the SMBH sphere of influence of radius $R_{\rm B}$ to the SMBH of gravitational radius $R_{\rm g}$ at the largest scale separation, $R_{\rm B}/R_{\rm g} = 10^3$, to date. Initially, our axisymmetric system of constant-density hot gas contains a weak vertical magnetic field and rotates in the equatorial plane of a rapidly spinning SMBH. We seed the gas with small-scale 2% level pressure perturbations. Infalling gas forms an accretion disk, and the SMBH launches relativistically magnetized collimated jets reaching well outside $R_{\rm B}$. Under the pressure of the infalling gas, the jets intermittently turn on and off, erratically wobble, and inflate pairs of cavities in different directions, resembling an X-shaped jet morphology. Synthetic X-ray images reveal multiple pairs of jet-powered shocks and cavities. Large-scale magnetic flux accumulates on the SMBH, becomes dynamically important, and leads to a magnetically arrested disk state. The SMBH accretes at 2% of the Bondi rate ($\dot{M} \simeq 2.4 \times 10^{-3} M_\odot$ yr^{-1} for M87*) and launches twin jets at $\eta = 150\%$ efficiency. These jets are powerful enough ($P_{\rm jets} \simeq 2 \times 10^{44}$ erg s^{-1}) to escape along the SMBH spin axis and end the short-lived intermittent jet state, whose transient nature can account for the rarity of XRGs.

Unified Astronomy Thesaurus concepts: High energy astrophysics (739); Active galactic nuclei (16); Black hole physics (159); Jets (870); Magnetohydrodynamical simulations (1966); General relativity (641)

1. Introduction

Modeling how the interstellar medium (ISM) or intercluster medium (ICM) reaches from the outskirts of a galaxy or cluster of galaxies down to the central supermassive black hole (SMBH) remains an unsolved, grand challenge problem. Observationally, it is clear that some poorly constrained fraction of the gas makes it down all the way to the SMBH, forms an accretion disk, and powers an active galactic nucleus (AGN). Such systems can produce copious radiation and mechanical outflows, broad winds, and tightly collimated relativistic jets. The jets can propagate through the galaxy, generate shocks, inflate bubbles, and heat up the surrounding medium (Zhuravleva et al. 2016; Martizzi et al. 2019; Li et al. 2020). It is commonly accepted that jet launching near the event horizon is powered by the extraction of the black hole (BH) rotational energy (Blandford & Znajek 1977). The jets initially align with the BH spin axis (McKinney et al. 2013), but interactions with the disk outflows can redirect the jets to follow the angular momentum of the accretion disk (Liska et al. 2018). Thus, the jet direction is determined by the complex interplay between the properties of the BH and its feeding.

A small, but significant, ~5%–10%, fraction of observed radio galaxies displays an intriguing X-shaped morphology, suggesting the presence of two pairs of jets at different orientations (Leahy & Williams 1984; Yang et al. 2019). Such X-shaped radio galaxies (XRGs) have been hypothesized to emerge due to (i) restarted activity of the central BH producing jets with different orientation (Bruni et al. 2019, 2020), (ii) jet deflection by the hot and oblique halo/ISM of the galaxy (Cotton et al. 2020), (iii) the presence of an SMBH binary, each component producing its own pair of jets (Lal & Rao 2007), (iv) reorientation of the SMBH spin axis due to SMBH coalescence (Merritt & Ekers 2002; Roberts et al. 2015), and (v) precession of the jet axis (Parma et al. 1985), due to e.g., Lense–Thirring precession of a tilted accretion disk (Liska et al. 2018). These might not be the only scenarios for forming the X-shaped morphology, and combinations of these are also plausible.

The goal of this work is to investigate whether X-shaped jet morphology can emerge spontaneously, without the above special, preexisting conditions. To reach the SMBH, the gas needs to make its way from the ISM/ICM, located outside the sphere of influence of the SMBH, or the Bondi radius $R_{\rm B} = GM_{\rm BH}/c_\infty^2 \sim 20$ pc $\times (M_{\rm BH}/10^9 M_\odot)$, at which the thermal pressure is high enough to counter the freefall of the gas (Bondi 1952), down to the scale of the gravitational radius, $R_{\rm g} = GM_{\rm BH}/c^2 = 5 \times 10^{-5}$ pc $\times (M_{\rm BH}/10^9 M_\odot)$. Here, $M_{\rm BH}$ is

the SMBH mass and c_∞ is the sound speed in the ISM/ICM. Galaxy simulations have been able to follow the gas flow down to ∼1 kpc (e.g., Anglés-Alcázar et al. 2015, 2017) and even subparsec scales in hyperrefined Lagrangian simulations (Anglés-Alcázar et al. 2021), approaching and even reaching inside the Bondi sphere. However, the event horizon is still orders of magnitude below the parsec scale, demanding dedicated numerical effort to bridge this gap in scale separation.

The simplest description of accretion is the spherically-symmetric analytic Bondi (1952) model, which does not include any rotation. Bondi accretion with nonzero angular momentum has been simulated by multiple groups (e.g., Proga & Begelman 2003a, 2003b; Cunningham et al. 2012; Li et al. 2013; Suková & Janiuk 2015; Suková et al. 2017; Xu & Stone 2019; Kaaz et al. 2019; Palit et al. 2019; Waters et al. 2020), often utilizing axisymmetric, nonrelativistic, hydrodynamic simulations. Accretion from a realistic ISM will be necessarily magnetized and have at least some angular momentum support. Thus, it is important to model both rotation and magnetic fields. Rotation breaks the symmetry of the problem, provides centrifugal support, and tends to enhance mass outflows, reducing the mass reaching the BH (Blandford & Begelman 2004; Begelman 2012). Magnetic fields are important, as they form magnetically powered outflows that can inject energy into the ambient gas. It is also crucial to include general-relativistic (GR) effects, in order to accurately represent the energy and momentum feedback by the central SMBH via launching BH-powered jets and disk-powered winds and to properly account for the poorly understood effects the BH has on the inner boundary condition of the flow. It is also critical to extend the studies to 3D, to model the essentially nonaxisymmetric magnetized turbulence, the associated angular momentum transport in the accretion disk, and to account for the development of 3D magnetic kink instabilities in the jets (see also Ressler et al. 2021; Kaaz et al. 2022; Jia et al. 2022). Tchekhovskoy & Bromberg (2016) initiated relativistic jets by magnetized rotation at the inner grid boundary of radius $R_{\rm B} = 0.1$ kpc and followed their propagation through the ISM over distances of tens of kpc for long durations, sufficient for the instabilities to develop. They found that the jets inflated cavities, morphologically similar to M87* and other low-luminosity AGN as seen, e.g., by Chandra (Forman et al. 2017). Barniol Duran et al. (2017) showed that the jets can undergo internal 3D kink instabilities and dissipation triggered by the change in the radial density profile at the Bondi radius (Russell et al. 2015).

Incorporating all of these effects, 3D GRMHD simulations are unique tools enabling self-consistent studies of gas accretion from the Bondi scale, including the formation of a turbulent accretion disk, the launching of relativistic jets, and the development of 3D magnetic kink instabilities that can dramatically affect the jet morphology and the state of the ambient gas. Despite the success of GRMHD simulations, direct modeling of 3D accretion spanning the full range of $\log_{10}(R_{\rm B}/R_{\rm g}) \simeq$ 5–6 orders of magnitude in distance (and 8–9 orders of magnitude in time) between the BH and Bondi scales still remains computationally prohibitive. Our approach is to reduce the scale separation to the maximum that is computationally feasible. While the scale separation is smaller than in reality, the more orders of magnitude it spans, the closer the flows can approach a self-similar regime that approximates nature. By varying the degree of scale separation, we can evaluate the effects our particular choices for the $R_{\rm B}/R_{\rm g}$ ratio have on the structure of the flow and analytically extend the results to the values of $R_{\rm B}/R_{\rm g}$ ratio found in nature.

In this Letter, we present the results of the first 3D GRMHD simulation that follows the accretion of an initially magnetized rotating gas with a scale separation of $R_{\rm B}/R_{\rm g} = 10^3$, which in 3D GRMHD is the largest to date and close to the maximum possible value attainable with current computational resources when evolved over astrophysically interesting times. We note that past works have simulated larger scale separations using a "two-zone" modeling, where the simulations near the BH were initialized using simulations at larger scales (Yuan et al. 2012; Ressler et al. 2020). Although this method successfully bridges the extreme/realistic scale separation to the environment near the BH, it cannot include a self-consistent feedback process originating from the jets/outflows that propagate from the inner to the outer regions and can alter the boundary conditions set by the large-scale simulations. Starting with the simplest, axisymmetric state of constant density, rotational profile of the gas, and vertical magnetic fields outside $R_{\rm B}$, we evolve the system until the formation of an accretion disk and a pair of relativistic jets and their interaction with the ambient gas. In Section 2 we present the numerical setup and the physical parameters of our model, and in Section 3 we present the results: the emergence of the X-shaped morphology (Section 3.1), the jet shape (Section 3.2), and synthetic X-ray images (Section 3.3). In Section 4 we conclude. We use units of $G = M = c = 1$.

2. Setup

We carry out a 3D GRMHD simulation using our GPU-accelerated GRMHD code H-AMR (Liska et al. 2019; see Porth et al. 2019 for comparisons with other GRMHD codes). We employ spherical polar coordinates, r, θ, φ, and choose a spherical polar grid that is uniform in $\log r$, θ, and φ variables. The grid spans the range of $(0.97R_{\rm g}, 10^5R_{\rm g}) \times (0, \pi) \times (0, 2\pi)$ and has the resolution of $N_r \times N_\theta \times N_\varphi = 192 \times 256 \times 128$ cells in the r, θ, and φ directions, respectively. We choose it such that the first five radial cells are inside the event horizon: This ensures that the BH exterior is causally disconnected from the inner radial grid boundary. We use outflow boundary conditions in the radial, transmissive conditions in the polar, and periodic conditions in the azimuthal directions (described in the supplementary information of Liska et al. 2019). We adopt axisymmetric initial conditions described by the following physical parameters:

(i) Density profile: Outside the Bondi radius, we set the ambient density to a uniform value of $\rho_\infty = 1$. Because the simulation includes neither the cooling (radiation) nor self-gravity effects, the results are scale-free in density: the simulation results can be freely rescaled to any value of ρ_∞. Within the Bondi radius, we place an empty cavity. The reason for this is we do not want to impose an initial density profile that may influence the subsequent steady-state solution.

(ii) Bondi radius: As we discuss in Section 1, in order to make the simulations affordable computationally, we choose a smaller $R_{\rm B}$ than inferred from observations ($R_{\rm B} \sim 10^5 - 10^6 R_{\rm g}$). Namely, we adopt a value of $R_{\rm B} = 10^3 R_{\rm g}$: This is the largest scale separation between $R_{\rm B}$ and $R_{\rm g}$ that has ever been achieved in 3D GRMHD that we are aware of, yet it still allows us to evolve the system for astrophysically interesting times. When discussing large-scale jet propagation outside $R_{\rm B}$, we convert the simulated lengths and times to physical lengths and times

by associating the Bondi scale and its light-crossing time in simulation units, $R_{\rm B} = 10^3 R_{\rm g}$ and $R_{\rm B}/c = 10^3 R_{\rm g}/c$, with those in the physical units for M87*, $R_{\rm B} = 0.15$ kpc and $R_{\rm B}/c = 0.15\,{\rm kpc}/c = 475$ yr, respectively (Russell et al. 2015). Our choice of $R_{\rm B}/R_{\rm g}$ naturally sets the sound speed in the ambient gas, $c_s = (R_{\rm B}/R_{\rm g})^{-1/2} c = 10^{-3/2} c \approx 0.03c$. We adopt a nonrelativistic ideal gas equation of state, $p_{\rm g} = (\gamma - 1) u_g$, where $\gamma = 5/3$ is the polytropic index for a monatomic gas, and $u_{\rm g}$ and $p_{\rm g}$ are the gas internal energy density and pressure as measured in the comoving frame of the gas.

(iii) Circularization radius: We assign a rotational profile to the gas, such that on each spherical shell of radius r, the gas undergoes solid-body rotation at the angular velocity, $\omega = l_0/r^2$, around the z-axis. Here, l_0 characterizes the specific angular momentum of the gas in the equatorial plane. We choose $l_0 =$ constant, such that the gas specific angular momentum, $l \simeq l_0 \sin^2\theta$, reaches its maximum value at the equatorial plane and smoothly drops down to zero near the poles (see also Palit et al. 2019).[6]

The value of l_0 depends on the circularization radius, $R_{\rm circ}$, at which the angular momentum in the equatorial plane equals the local Keplerian value. We adopt

$$R_{\rm circ} = l_0^2/(GM_{\rm BH}) = 30 R_g, \tag{1}$$

which divides approximately equally the scale separation between $R_{\rm g}$ and $R_{\rm B}$ and results in sub-Keplerian rotation at the Bondi radius, $l_0/l_{\rm K}(R_{\rm B}) = (R_{\rm circ}/R_{\rm B})^{1/2} \approx 0.17$.

(iv) Initial gas magnetization: We adopt the initial magnetic field threading the gas to be asymptotically a homogeneous vertical magnetic field in the z direction and initialize it by setting the covariant magnetic vector potential, which has only one nonzero component: $A_\varphi = (r^2 - R_{\rm B}^2)\sin^2\theta$ at $r \geqslant R_{\rm B}$ and 0 otherwise. This ensures that A_φ and the magnetic field vanish inside $R_{\rm B}$ and do not bias the formation and evolution of the accretion flow there. Physically, the covariant φ component of the vector potential, A_φ, gives the poloidal (pointing in the r and θ directions) magnetic flux enclosed by an axisymmetric ring, (r, θ), divided by 2π. We characterize the strength of the magnetic field via the plasma-β parameter, defined as the ratio of thermal to magnetic pressure, $\beta = p_{\rm g}/p_{\rm m}$, where $p_{\rm m}$ is the magnetic pressure. We normalize the magnetic field strength by choosing the characteristic value of the plasma β to be high enough so that the initial accretion stage is gas pressure dominated, $\min \beta = 100$.

(v) BH spin: We consider a rapidly spinning BH, with high dimensionless spin, $a = 0.9375$, to give the jets the best chance to form and survive in their fight against the onslaught of the infalling gas: If the jets form, their power will be close to the maximum possible value for a given magnetic flux ($P_{\rm jets} \propto a^2$, Blandford & Znajek 1977), enabling us to study the physics of their interaction with the infalling gas.

We add to the initial pressure random perturbations (independent for each numerical cell) at the level of 2%: Without the perturbations, the system would maintain the exact axisymmetry and its evolution would be identical to a 2D model. We then let the system evolve out to $t = 2.3 \times 10^5 R_{\rm g}/c = 230 R_{\rm B}/c = 0.1$ Myr and report the simulation results.

[6] Here, $l = u_\varphi \equiv g_{\varphi\mu} u^\mu \approx r^2 \sin^2\theta\, d\varphi/dt$ is the φ component of the covariant four-velocity, a conserved quantity for test particles in the Kerr spacetime (we evaluated the approximate equality above in the nonrelativistic limit and flat space).

3. Results

3.1. Natural Development of the X-shaped Jet Morphology

The simulation starts[7] with a uniform gas distribution outside the Bondi radius, and a vacuum hole at $r < R_{\rm B}$. The gravitational forces along with the pressure gradient at the interface of the hot gas and the empty cavity, at $r = R_{\rm B}$, push the gas inward. Because the gas possesses a nonzero angular momentum (Section 2), it undergoes what is nearly a freefall until it hits the centrifugal barrier at $R_{\rm circ} = 30\,R_{\rm g}$. At this point, the radial infall slows down, and inside $R_{\rm circ}$ an accretion disk forms. Because on the way to the BH the gas spends most of the time at the largest distances, we can estimate the time it takes for it to travel from $R_{\rm B}$ to the BH as the freefall time, $t_{\rm ff} = 2^{-1/2}(R_{\rm B}/R_{\rm g})^{3/2} R_{\rm g}/c \approx 2.2 \times 10^4 R_{\rm g}/c$. As seen in Figure 1(a), around $t_{\rm ff}$, the mass accretion rate $\dot{M}$ reaches its first peak and oscillates thereafter. Here, $\dot{M} = -\iint \rho u^r dA$, where $dA = \sqrt{-g}\, d\theta d\varphi$ and $g = |g_{\mu\nu}|$ is the determinant of the metric. Analogously, we define the energy accretion rate, $\dot{E} = \iint [(\rho + u_g + p_g + 2p_{\rm m}) u^r u_t - b^r b_t/4\pi] dA$, where b^μ is the fluid-frame magnetic field 4-vector. We evaluate both $\dot{M}$ and $\dot{E}$ at $r = 5R_{\rm g}$ to avoid potential contamination by the density floors near the horizon. Because in a steady state $\dot{M}$ and $\dot{E}$ are conserved and independent of radius, this does not affect time-average values and only slightly shifts the dependencies in time by $\Delta t \lesssim 5R_{\rm g}/c$, i.e., shorter than the sampling time of the simulation.

We use the sign convention such that positive $\dot{M}$ and $\dot{E}$ imply mass and energy entering the BH. We define the outflow energy efficiency as $\eta = (\dot{M}c^2 - \dot{E})/\dot{M}c^2$. The gas drags with it the magnetic flux, and as Figure 1(b) shows, this leads to an increase in the absolute magnetic flux on the BH, $\Phi_{\rm BH} = 0.5 \iint |B^r|\, dA$, where the integration is over the area of the event horizon. We further normalize the magnetic flux by the time-smoothed mass accretion rate, $\phi_{\rm BH} \equiv \Phi_{\rm BH}/(\dot{M} R_{\rm g}^2 c)^{1/2}$. We smooth all quantities in Figure 1 over a timescale of $1000 R_{\rm g}/c$ using a zeroth-order Savitzky–Golay filter to make the plots more readable.

As the accretion disk forms, the magnetized rotation of the BH works to form highly magnetized jets. The increasing magnetic flux on the BH would ordinarily translate into magnetically powered jets via the Blandford & Znajek (1977, BZ, hereafter) effect. However, the BH is engulfed in the infalling gas from all directions, which suppresses the event horizon electromagnetic (EM) luminosity of the jets, L, well below the analytic BZ expectation, $L_{\rm BZ}$: Figure 1(c) shows that $L/L_{\rm BZ} \lesssim 0.25$ at $t \lesssim 5 \times 10^4 R_{\rm g}/c$. In order for the jets to successfully launch and avoid falling apart due to gas–jet interaction and the development of magnetic kink instabilities, their total pressure needs to be higher than approximately the ram pressure of the infalling gas (Gottlieb et al. 2022). This happens only when the BH horizon accumulates enough magnetic flux, which powers the jets along with the spin of the BH, via the BZ process. When the jets work intermittently, we find that the fluctuation of the magnetic flux on the BH is accompanied by polarity flips, similar to Christie et al. (2019); this will be investigated in future work.

[7] Relevant movies available here.

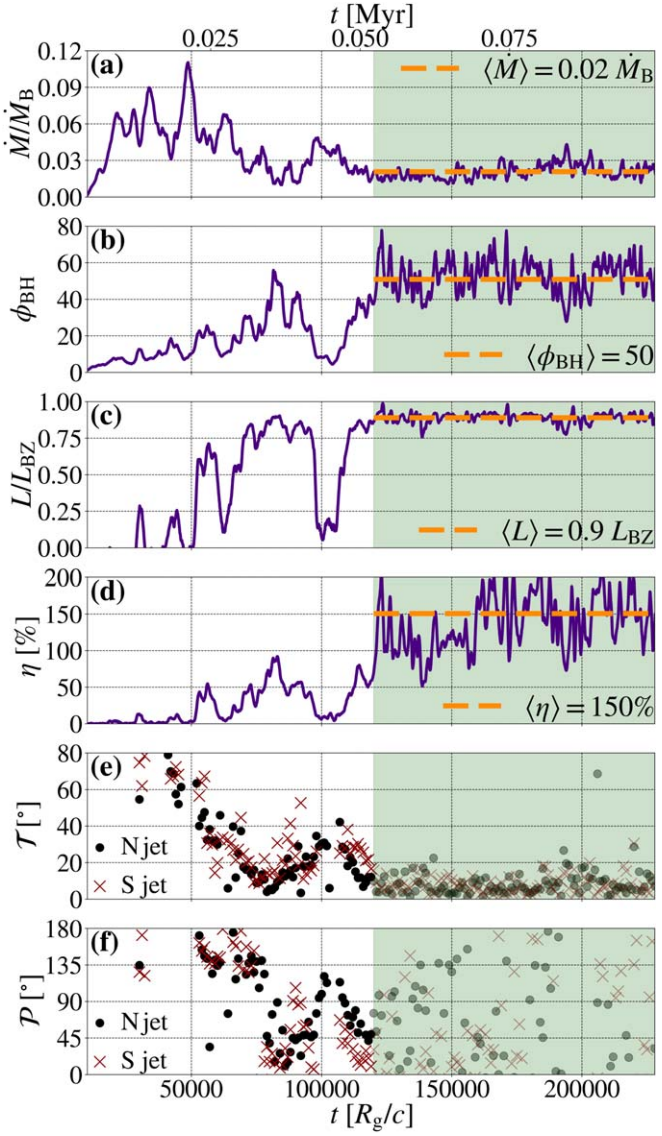

Figure 1. To survive the onslaught of infalling gas, jets deflect toward the equatorial plane ($\mathcal{T}\sim 90^\circ$, panel e), before aligning with the z-axis ($\mathcal{T}\lesssim 10^\circ$). This jet reorientation naturally results in an X-shaped jet morphology (Figure 2). The early period, $t\leqslant 5\times10^4 R_g/c$, of high mass accretion rate $\dot{M}/\dot{M}_B\gtrsim 0.06$ (panel a) features low values of the dimensionless BH magnetic flux $\phi_{BH}\lesssim 20$ (panel b), total-EM to BZ jet-power ratio $L/L_{BZ}\lesssim 0.25$ (panel c), and jet energy efficiency $\eta\lesssim 10\%$ (panel d). The infalling dense gas easily deflects the weak jets sideways, toward the equatorial plane, resulting in high jet-tilt angle $\mathcal{T}\sim 90^\circ$ (panel e) and large variations, $\sim$180°, in precession $\mathcal{P}$ angle (panel f). At later times, $t\gtrsim 10^5 R_g/c$, the accumulation of large-scale vertical magnetic flux on the BH leads to strong $\phi_{BH}\sim 50$ (panel b) and a MAD state (highlighted in green; steady-state averages shown with horizontal dashed orange lines): The powerful jets, $L/L_{BZ}\sim 1$ (panel c) and $\eta\sim 150\%$ (panel d), suppress $\dot{M}$ (panel a) and stably propagate along the z-axis ($\mathcal{T}\lesssim 10^\circ$, panel e), about which both the BH and the ambient gas rotate, out to large distances (Figures 2 and 4). When jets are nearly aligned, the value of the precession angle is not well defined, resulting in noisy values. During the MAD state, $\dot{M}$ saturates at 2% of $\dot{M}_B$ (panel a), implying that only 2% of the Bondi accretion rate reaches the BH and the rest, 98%, leaves as outflows.

Figures 1(b) and (c) show that, apart from a few bumps, the magnetic flux steadily increases until $t\lesssim 10^5 R_g/c$, and L/L_{BZ} displays several prominent peaks reaching near unity. Figure 1(a) shows that the dips in $\dot{M}$ correlate with the spikes in the magnetic flux, luminosity, and efficiency in Figures 1(b)–(d). These are the moments when the jets are successfully launched with $\eta\sim 50\%$ before drops in ϕ_{BH} disrupt them.

To better understand the behavior of the jets, we determine their tilt $\mathcal{T}$ and precession $\mathcal{P}$ angles by computing the polar and azimuthal centroid positions, respectively, for both the northern and southern jets. For this, we introduce the total-energy to mass-energy flux ratio, $\mu=-u_t(h+\sigma+1)$ (Chatterjee et al. 2019), which gives the maximum Lorentz factor the flow could attain if all of its energy is converted into kinetic energy. Here $u_t=g_{t\nu}u^\nu$ is the covariant time component of the 4-velocity, $h=(u_g+p_g)/(\rho c^2)$ is the specific enthalpy, and $\sigma\approx 2p_m/(\rho c^2)$ is the magnetization. We identify the jets on a sphere of radius $50R_g$ using the condition $\mu\geqslant 2$, which selects the relativistic regions (jets) and eliminates non- and mildly relativistic regions (accretion flow and mildly relativistic outflows). Surprisingly, Figures 1(e)–(f) show that jet tilt and precession angles vary strongly as the jets erratically launch. In fact, at early times, $t\lesssim 5\times10^4 R_g/c$, the jets launch nearly perpendicular to the polar axis, essentially in the equatorial plane. We see a clear anticorrelation between the inclination and precession angles (Figures 1(e)–(f)) and the energy efficiency of the jets (Figure 1(d)): When η peaks at $t\sim 7.5\times10^4 R_g/c$, both $\mathcal{T}$ and $\mathcal{P}$ drop. Conversely, as η drops at $t\sim 10^5 R_g/c$, both $\mathcal{T}$ and $\mathcal{P}$ increase. This suggests that weaker jets are more easily deflected sideways by the pressure of the infalling gas.

Figures 2(a)–(e) shows that the jets, which appear as underdense yellow-green regions, indeed propagate nearly horizontally away from the center. Their launch direction strongly deviates from that of the BH spin and ambient gas angular momentum vector directions, both of which are vertical and point along the z-axis. Shortly after launch, the jets subsequently quench. The timescale between the launching and quenching of the jets is approximately $t\sim 10^4 R_g/c$, or $\sim$0.01 Myr when rescaled to M87*.

Later on, at $t\gtrsim 10^5 R_g/c$, Figures 1(a)–(d) shows that the jet efficiency increases, and all quantities settle around their respective asymptotic values. The accretion rate reaches the low value of $\langle\dot{M}\rangle/\dot{M}_B=0.02$ in units of the analytic spherical Bondi accretion rate, while the magnetic flux asymptotes at the value $\langle\phi_{BH}\rangle=50$. During this time, the near-BH region reaches inflow equilibrium. By the end of the simulation, the size of the inflow equilibrium region has reached a distance of $\sim 250R_g$. Future work will include longer-duration simulations to test if these results change as the equilibrium region reaches the Bondi radius. The jet power levels off at $\langle L\rangle=0.9\,L_{BZ}$ with an outflow efficiency reaching $\langle\eta\rangle=150\%$. Figure 1 shows these steady-state average values with horizontal dashed orange lines. Figure 1(e) shows that the jets manage to avoid getting deflected by the infalling gas and launch with a near-zero tilt along the vertical z-axis. We can also see this in Figures 2(c)–(i), which show the jets propagating vertically outwards, displaying only slight bends, producing powerful backflows, and maintaining their overall stability. The above high values of the dimensionless BH magnetic flux, jet luminosity, and efficiency, as well as the ability of the jets to avoid getting deflected by the infalling gas, make it clear that the jets are now strong enough to overcome the destructive effects of the infalling gas and operate at full strength. In fact, such high dimensionless magnetic flux and efficiency values of $\phi_{BH}\simeq 50$, $\eta\gtrsim 100\%$, are characteristic of the magnetically arrested disk (MAD) state in which the large-scale vertical magnetic flux saturates the BH, and the magnetic field becomes strong

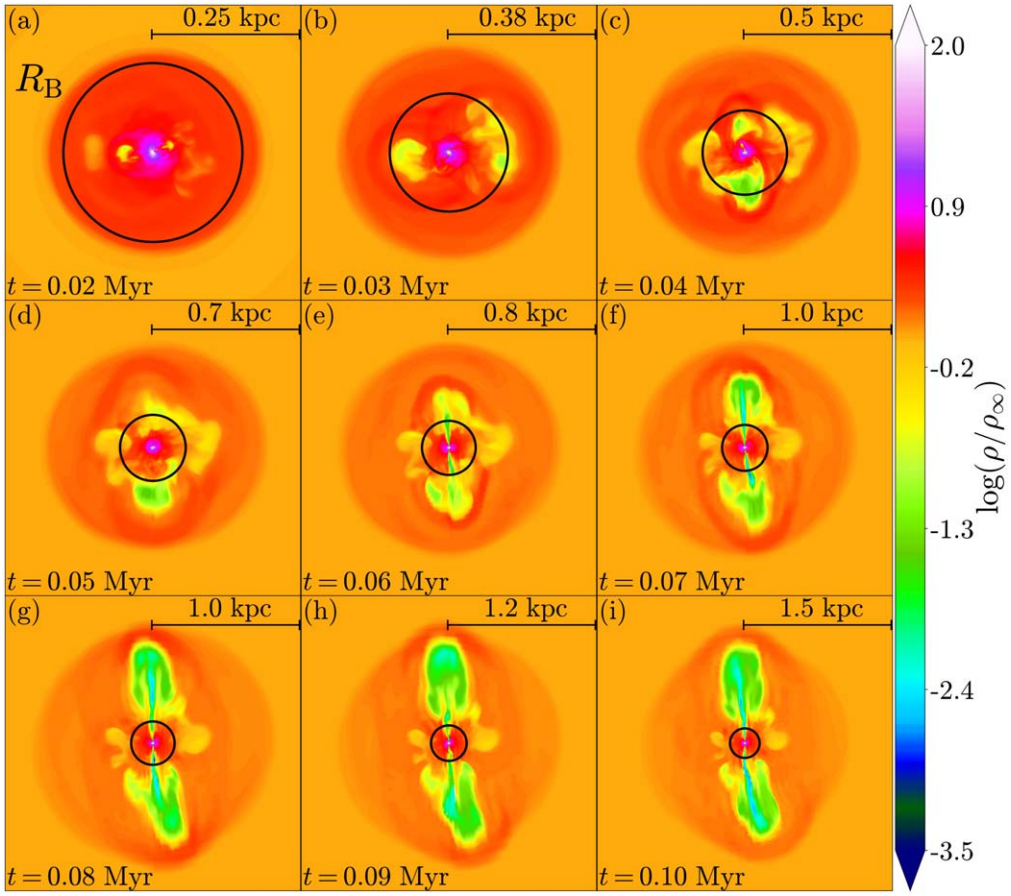

Figure 2. The first demonstration that X-shaped radio galaxy morphology naturally emerges from initially axisymmetric conditions: BH and ambient gas initially rotate around the vertical z-axis, with the gas threaded by a vertical magnetic field. Panels (a)–(i) show a time sequence of vertical slices through the simulated density (see color bar). The times and lengths shown in each panel have been scaled to M87*: 0.15 kpc $= R_{\rm B} = 10^3 R_{\rm g}$, 475 yr $= R_{\rm B}/c = 10^3 R_{\rm g}/c$. The early-time $t \lesssim 10^5 R_g/c \sim 0.05$ Myr evolution results in intermittent low-density jets (seen in yellow-green) that are frequently disrupted due to the onslaught of infalling gas and transient reductions in jet power (see also Figure 1). In spite of this, the jets and cavities they inflate manage to reach outside the Bondi radius, which is shown with a black circle. Throughout the simulation, jets and remnant cavities point in different directions and resemble the X-shaped jet morphology in XRGs. The jets stabilize around $t \sim 10^5 R_g/c \sim 0.05$ Myr, once the BH saturates with the vertical magnetic flux and the disk enters the MAD state: The jets become strong enough to avoid getting deflected by the infalling gas and propagate along the vertical z direction. This ends the short-lived intermittent jet state, whose transient nature can account for the rarity of XRGs.

enough to periodically overcome the gravity pulling in the accreting gas and escape from the BH (Tchekhovskoy et al. 2011). These repeating magnetic flux eruptions manifest themselves through the fluctuations of the magnetic flux and jet efficiency in Figures 1(b) and (d) at $t \geqslant 10^5 R_{\rm g}/c$. For the rest of the simulation, we do not see any activity that indicates any deviation from this steady state, although the rest of the duration is as long as the early-time intermittent jet state. We anticipate that whenever the BH magnetic flux and jet power dip (e.g., due to the accretion of opposite-polarity magnetic flux), the jets will develop a significant misalignment (similar to $t \sim 10^5 R_{\rm g}/c$).

The formation of wobbling jets is in contrast with the general expectation that when the BH spin and accreting gas angular momentum vectors are aligned, the accretion disk produces jets that propagate along their common direction. The reason for the jet wobble lies in the interaction with the surrounding gas, which deflects the jet head. This implies that even though the early-time wobbling behavior of the jets might be a transient phenomenon, its effects can be long-lasting and potentially probed through low-density cavities in the surrounding medium. The resulting morphology remarkably resembles the strongly asymmetric X-shaped jet morphology of XRGs (Section 1), even though the initial setup is axisymmetric about the z-axis, apart from 2% level pressure perturbations. Figure 3 shows a 3D volume rendering of the system illustrating the development of the X-shaped morphology. We note that differences in the magnitude or spatial distribution of the ambient medium angular momentum can affect (or even suppress) the jet misalignment and wobbling; we will study this in future work.

Because a realistic ISM has much stronger pressure fluctuations, any jet wobbling seen here will be much more pronounced for realistic ambient media. Transient drops in $\phi_{\rm BH}$ can shut off jet outbursts, and subsequent magnetic flux accumulation periods can power a newly formed pair of jets in a different direction. Eventually, enough magnetic flux accumulation on the BH leads to a MAD state (Tchekhovskoy et al. 2011), and the power of the jet reaches its maximum value and manages to overcome the ambient gas density. In Figures 2(e)–(i), the system is in the MAD state, and not only do the newly formed jets remain stable in the highest-density regions close to the BH, they also retain their stability all the way out to $\sim$7000 $R_{\rm g} \simeq 1$ kpc. Note that the jet half-opening angle at these large scales is marginally resolved by about

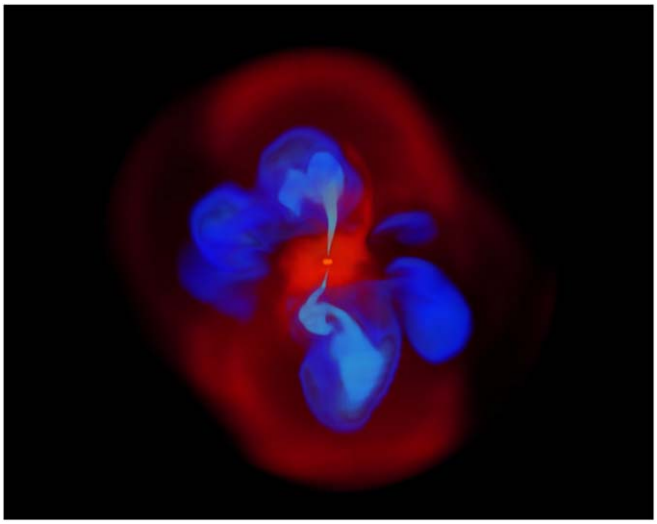

Figure 3. Three-dimensional volume rendering of density at $t = 1.2 \times 10^5 R_g/c \simeq 0.05$ Myr (see Figure 2(d)) illustrates the natural development of X-shaped jet morphology. Gas infall forms an accretion flow (bright red) and launches a pair of relativistic jets (light blue), which propagate vertically and shock the ambient gas (dark red). The older cavities (dark blue), which were inflated by previous misaligned jet activity, buoyantly rise at an angle to the vertically propagating jets, form the X-shaped jet morphology.

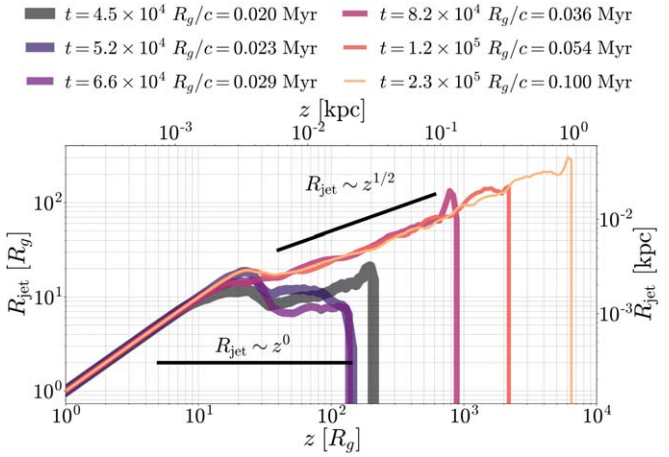

Figure 4. Northern jet transitions from cylindrical shape at early times to parabolic shape at late times (southern jet shows qualitatively similar behavior; not shown). Lines of different colors and thicknesses indicate different times (see legend). At early times, $t \lesssim 0.03$ Myr, the jets exhibit a cylindrical shape at $z \gtrsim 10R_g$: the ram pressure is high (large $\dot{M}$ in Figure 1(a)) and BH magnetic flux and jet power are low (small $\phi_{\rm BH}$ and η in Figures 1(b) and (d)), leading to strong collimation of the jets. At later times, after enough magnetic flux has accumulated on the BH, the jets become stronger and take on a parabolic shape. We compute the cylindrical radius of the jet via the solid angle subtended by the jet (which we identify here as the region of $\mu > 1.5$).

seven cells; at higher numerical resolutions, the jets might show more signs of 3D kink instability.

3.2. Cylindrical and Parabolic Jets

Jets propagating through a dense medium can have rather different shapes and stability compared to jets in a vacuum. Observations indicate that AGN jets often show a transition from a parabolic shape inside to a conical shape outside the Bondi radius (Nakamura & Asada 2013; Kovalev et al. 2020; Boccardi et al. 2021). The origin of such a transition could either be due to the internal jet evolution (e.g., Nokhrina et al. 2020) or changes in the ambient density profile (e.g., Barniol Duran et al. 2017).

Figure 4 shows the effective cylindrical radius of the northern jet, implied by the solid angle it subtends, versus the distance along the jet (the shape of the southern jet is similar and not shown). Because we use a logarithmic grid, at $r \gtrsim 4000R_g$ numerical diffusion in the jets increases the mixing, and thus we loosen our jet condition to $\mu \geqslant 1.5$. In the very early intermittent jet phase, $t \lesssim 7 \times 10^4 R_g/c = 0.03$ Myr, the jet is approximately cylindrical, $R_{\rm jet} \sim$ constant. At later times, while still in the early phase and substantially tilted relative to the z-axis, the jet transitions to a parabolic shape, $R_{\rm jet} \propto z^{1/2}$. The parabolic shape persists to late times, and the jets stably propagate from the BH along the z-axis out to $z \sim 7000R_g = 7R_B \simeq 1$ kpc, without showing any telltale signs of disruptive kink-instability. Although the jets leave the Bondi sphere, they do not appear to exhibit the transition from parabolic to conical geometry at the Bondi radius. It is possible that longer and higher-resolution simulations will show both the jet disruption due to the kink instability (for ambient medium density profiles shallower than $\rho \sim r^{-2}$, magnetized jets become progressively more kink-unstable as they propagate; Tchekhovskoy & Bromberg 2016; Bromberg & Tchekhovskoy 2016) and the parabolic-to-conical transition, when the backflows are no longer able to reach from the jet head back to R_B and affect the jet shape there.

3.3. Shocks and Cavities in Synthetic X-ray Images

Each panel of Figure 2 indicates the position of the Bondi radius with a black circle and the spatial extent of the system with a black scale bar. Figure 2 shows that gas infall launches an expanding spherical accretion shock that forms as the gas finds itself rushing to the BH too fast. The shock reduces the gas radial infall velocity and helps the system to reach a steady state. Jets drive into the ambient gas an additional pair of bow shocks that, by the end of the simulation, elongate the accretion shock in the polar directions and start outrunning it.

The accretion and jet bow shocks compress and heat the ambient medium, resulting in thermal bremsstrahlung X-ray emission. We are presenting a crude estimate of what the X-ray emission would look like by calculating the bremsstrahlung bolometric emissivity, which scales as $P_X \sim \rho^2 T^{1/2}$ for fully ionized hydrogen. We assume an optically thin gas and do not include any absorption or scattering effects. To construct synthetic X-ray images, we calculate the emissivity and compute its projection along the desired line of sight.

Columns in Figure 5 depict a time series of synthetic X-ray bolometric emissivity images. To highlight structure, we normalize the emissivity by its angle-averaged radial profile. Rows show views at different inclination angles relative to the z-axis, $i = [15, 30, 90]°$. At early times, in both the left and middle columns, both accretion shock and bow shocks are visible, leading to an emissivity increase of ≈5%–20% compared to the angle average (see the color bar). The bow shock encompasses the bulk of excess X-ray emissivity and surrounds the newly formed jets. The dark regions show both the old jet-inflated cavities and newly formed jets. The jet-inflated low-density cavities buoyantly rise, slower than the jets, and are soon outrun by them. The resulting X-shaped morphology is especially prominent in Figures 5(b1), (b2), (c1), and (c2): Here, the jets are approximately at the same distance from the SMBH as the older, jet-inflated cavities, forming a distinct X-shape. Specifically, Figure 5(c2) is

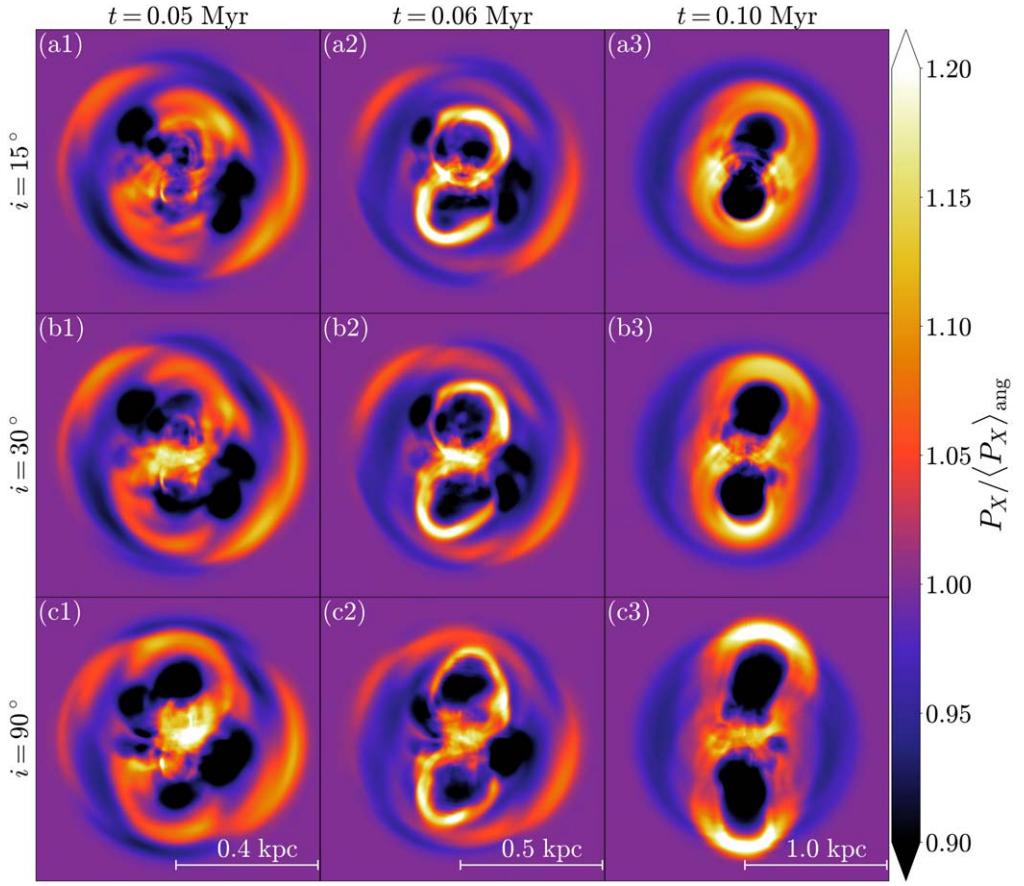

Figure 5. Synthetic bolometric X-ray images (emissivity $P_X \propto \rho^2 T^{1/2}$, ignoring absorption and scattering) demonstrate the formation of X-shaped jet morphology. Shock compressed and heated regions dominate the Bremsstrahlung emission, whereas empty cavities show jets or jet-inflated cavities. These low-emission regions present a morphology similar to X-shaped jets in XRGs. The color depicts the emissivity normalized by its angle-averaged value (Section 3.3). Each row and column corresponds to a different inclination angle and time, respectively. Times and lengths shown in each panel have been scaled to M87* (see also Figure 2).

visually similar to the pair of X-ray cavities observed in RBS 797 (Ubertosi et al. 2021) (see also Figure 3). In the right column, even though the bow shock has outrun the accretion shock and the jets have reached $\sim 7R_{\rm B} \simeq 1$ kpc, we can still see the old jet-inflated remnant cavities closer to the BH.

4. Summary and Discussion

We have presented the first-ever 3D GRMHD simulation of an SMBH accreting rotating magnetized ambient gas from outside the Bondi radius, at the largest scale separation of $R_{\rm B}/R_{\rm g} = 10^3$ to date in 3D GRMHD. Initially located outside an empty cavity of radius $R_{\rm B}$, the uniform-density ambient gas contains a weak vertical magnetic field in the z direction, which is aligned with both the BH spin and gas angular momentum vectors. As the gas falls in, it self-consistently forms a thick accretion disk whose size is set by the circularization radius of the ambient gas (Equation (1)). More generally, the properties of the accretion system are controlled by several manifestly physical dimensionless parameters (see Section 2): (i) dimensionless Bondi radius, $R_{\rm B}/R_{\rm g}$, (ii) dimensionless circularization radius, $R_{\rm circ}/R_{\rm g}$, (iii) ambient gas plasma β, and (iv) dimensionless BH spin, a. This offers certain advantages over the standard equilibrium torus initial conditions typically used in GRMHD simulations (Fishbone & Moncrief 1976; De Villiers & Hawley 2003), where the parameters of the torus are harder to relate to observables.

As the infalling gas approaches the sonic surface too fast, an accretion shock develops. Around the same time, $t \simeq 2 \times 10^4 R_{\rm g}/c$, a pair of low-density intermittent jets launch near the equatorial plane and get disrupted soon thereafter. The disrupted jet remnants form low-density bubbles, which buoyantly rise beyond the Bondi radius. The repetitive disruption and recreation of the jets can be caused by (i) variability in large-scale vertical flux on the BH horizon (Figure 1(b)), leading to jet power variability (Figure 1(d)) and even intermittent destruction of the jets; and (ii) high ram pressure of the infalling gas on the BH horizon overcomes the ram pressure of the jets at times of low jet power and deflects them toward the equatorial regions. Indeed, minima in $\phi_{\rm BH}$ and η in Figures 1(b) and (d) correlate with the times of jet destruction, $L/L_{\rm BZ} \ll 1$, seen in Figure 1(c). At early times, when the mass accretion rate is high (large $\dot{M}/\dot{M}_{\rm B} \sim 0.06$) and jet ram pressure and power are low ($\eta \lesssim 50\%$), the tilt and precession angles of our jets reach large values, $\mathcal{T} \sim 90°$ and $\mathcal{P} \sim 180°$ (Figures 1(e) and (f)), implying that the infalling gas has deflected the jets toward the equatorial plane, i.e., perpendicular to the z-axis. Figure 2 shows that these early-time intermittent equatorial jets inflate buoyant bubbles whose direction is misaligned relative to the late-time stable jets. The synthetic X-ray images in Figure 5 show multiple sets of jet-inflated cavities at different orientations. This morphology strongly resembles X-shaped jets in XRGs. Thus, the deflections of jets by infalling material can provide a natural

and simple explanation of XRG formation. Furthermore, the short-lived nature of the intermittent jet phase can explain the rarity of XRGs, which make up less than 1 in 10 radio galaxies.

At $t \gtrsim 10^5 R_g/c$, the BH accumulates so much magnetic flux that the system goes MAD ($\langle\phi_{BH}\rangle = 50$) and the jets attain the maximum power for a given mass accretion rate (Tchekhovskoy et al. 2011). Namely, the jet luminosity is comparable to the BZ power, $\langle L\rangle \sim L_{BZ}$ (Figure 1(c)), and the outflow energy efficiency reaches $\langle\eta\rangle = 150\%$ (Figure 1(d)). The accretion rate on the BH saturates at a level of $\langle\dot{M}\rangle = 0.02\dot{M}_B$ (Figure 1(a)), implying that 98% of the infalling gas at the Bondi radius is ejected from the system, with only 2% of the gas reaching the BH.

The Bondi accretion rate for M87* is

$$\dot{M}_B = 4\pi\lambda_s n_B m_p R_B^2 c (R_B/R_g)^{-1/2} \approx 0.12 M_\odot \mathrm{yr}^{-1} \times \frac{n_B}{0.17\ \mathrm{cm}^{-3}} \times \left(\frac{R_B}{150\ \mathrm{pc}}\right)^{3/2}, \quad (2)$$

where $\lambda_s = 1/4$ for $\gamma = 5/3$ (Shapiro & Teukolsky 1986; Di Matteo et al. 2003), and we assumed ionized hydrogen. Using this and the steady-state values for the system given above, the simulated mass accretion rate on the BH scaled to M87* becomes

$$\dot{M} = 2.4 \times 10^{-3} M_\odot\ \mathrm{yr}^{-1} \times \frac{\langle\dot{M}/\dot{M}_B\rangle}{0.02} \times \frac{\dot{M}_B}{0.12 M_\odot\ \mathrm{yr}^{-1}}, \quad (3)$$

which comes out near the high end of the inferred range for M87*, $\dot{M} = (3\text{–}20) \times 10^{-4} M_\odot\ \mathrm{yr}^{-1}$ (Akiyama et al. 2021), and the simulated power of two jets becomes

$$P_{jets} \simeq 2 \times 10^{44}\ \mathrm{erg\ s}^{-1} \times \frac{\langle\eta\rangle}{150\%} \times \frac{\langle\dot{M}/\dot{M}_B\rangle}{0.02} \times \frac{\dot{M}_B}{0.12 M_\odot\ \mathrm{yr}^{-1}}, \quad (4)$$

in agreement with the inferred range of the jet power, 10^{42}–$10^{45}\ \mathrm{erg\ s}^{-1}$ (e.g., Stawarz et al. 2006; Broderick et al. 2015; Prieto et al. 2016; Nemmen 2019); here we approximated the power of the two jets as the total outflow power. Our expectation is that as we increase the scale separation from $R_B/R_g = 10^3$ closer to more physically motivated values, 10^5–10^6, more gas will be ejected in outflows, less gas will reach the BH, and the agreement with the observations will improve.

We measure the shape of the jets to study whether our jets exhibit the parabolic to conical jet shape transition, which is observed near the Bondi radius in some AGNs (Nakamura & Asada 2013; Kovalev et al. 2020; Boccardi et al. 2021). Figure 4 shows that whereas early-time jets have a cylindrical shape, at later times, $t \simeq 6 \times 10^4 R_g/c$, the jets transition to a parabolic shape. We do not see any signs of transition from parabolic to conical. We will investigate this issue in the future by carrying out higher-resolution and longer-duration simulations, both of which might help reveal the transition in jet shape (Section 3.2).

We have only studied a limited parameter space, and we plan to expand it in future work by (i) choosing a physically motivated density profile, $\rho \propto r^{-1}$, outside the Bondi radius (Russell et al. 2015); (ii) varying the scale separation, R_B/R_g, and quantifying the differences in $\dot{M}/\dot{M}_B$; (iii) varying the circularization radius, R_{circ}/R_g, and studying the effects the size of the disk has on the accretion rate and outflow power; (iv) extending simulation durations to $t = 10^6$–$10^7 R_g/c$ potentially sufficient for the jets to transition to a conical shape and/or fall victims to instabilities and get disrupted; and (v) including radiation transport and the effects of cooling on the dynamics of the accretion and power of the outflows.

We thank Claude-Andre Faucher-Giguere and the anonymous referee for useful comments and suggestions. O.G. is supported by a CIERA Postdoctoral Fellowship. K.C. is supported by a black hole Initiative Fellowship at Harvard University, which is funded by grants from the Gordon and Betty Moore Foundation, John Templeton Foundation, and the Black Hole PIRE program (NSF grant OISE-1743747). A.T. was supported by BSF grant 2020747 and NSF grants AST-2107839, AST-1815304, AST-1911080, OAC-2031997. Support for this work was provided by the National Aeronautics and Space Administration through Chandra Award Number TM1-22005X issued by the Chandra X-ray Center, which is operated by the Smithsonian Astrophysical Observatory for and on behalf of the National Aeronautics Space Administration under contract NAS8-03060. The study of the jet shape (Figure 4) has been supported by the Russian Science Foundation, project 20-62-46021. The authors acknowledge the use of Frontera and Longhorn supercomputers (Stanzione et al.2020) of the Texas Advanced Computing Center (TACC) at The University of Texas at Austin for providing HPC and visualization resources that have contributed to the research results reported within this paper via the LRAC allocation AST20011 (http://www.tacc.utexas.edu). An award of computer time was provided by the Innovative and Novel Computational Impact on Theory and Experiment (INCITE) program under award PHY129. This research used resources of the Oak Ridge Leadership Computing Facility, which is a DOE Office of Science User Facility supported under contract DE-AC05-00OR22725. I.Z. is partially supported by a Clare Boothe Luce Professorship from the Henry Luce Foundation.

ORCID iDs

Aretaios Lalakos https://orcid.org/0000-0002-6883-6520
Ore Gottlieb https://orcid.org/0000-0003-3115-2456
Nicholas Kaaz https://orcid.org/0000-0002-5375-8232
Koushik Chatterjee https://orcid.org/0000-0002-2825-3590
Alexander Tchekhovskoy https://orcid.org/0000-0002-9182-2047
Irina Zhuravleva https://orcid.org/0000-0001-7630-8085
Elena Nokhrina https://orcid.org/0000-0002-3897-2417

References

Akiyama, K., Algaba, J. C., Alberdi, A., et al. 2021, ApJL, 910, L13
Anglés-Alcázar, D., Faucher-Giguère, C.-A., Quataert, E., et al. 2017, MNRAS, 472, L109
Anglés-Alcázar, D., Quataert, E., Hopkins, P. F., et al. 2021, ApJ, 917, 53
Anglés-Alcázar, D., Özel, F., Davé, R., et al. 2015, ApJ, 800, 127
Barniol Duran, R., Tchekhovskoy, A., & Giannios, D. 2017, MNRAS, 469, 4957
Begelman, M. C. 2012, MNRAS, 420, 2912
Blandford, R. D., & Begelman, M. C. 2004, MNRAS, 349, 68
Blandford, R. D., & Znajek, R. L. 1977, MNRAS, 179, 433
Boccardi, B., Perucho, M., Casadio, C., et al. 2021, A&A, 647, A67
Bondi, H. 1952, MNRAS, 112, 195

Broderick, A. E., Narayan, R., Kormendy, J., et al. 2015, ApJ, 805, 179
Bromberg, O., & Tchekhovskoy, A. 2016, MNRAS, 456, 1739
Bruni, G., Panessa, F., Bassani, L., et al. 2019, ApJ, 875, 88
Bruni, G., Panessa, F., Bassani, L., et al. 2020, MNRAS, 494, 902
Chatterjee, K., Liska, M., Tchekhovskoy, A., & Markoff, S. B. 2019, MNRAS, 490, 2200
Christie, I. M., Lalakos, A., Tchekhovskoy, A., et al. 2019, MNRAS, 490, 4811
Cotton, W., Thorat, K., Condon, J., et al. 2020, MNRAS, 495, 1271
Cunningham, A. J., McKee, C. F., Klein, R. I., Krumholz, M. R., & Teyssier, R. 2012, ApJ, 744, 185
De Villiers, J.-P., & Hawley, J. F. 2003, ApJ, 592, 1060
Di Matteo, T., Allen, S. W., Fabian, A. C., Wilson, A. S., & Young, A. J. 2003, ApJ, 582, 133
Fishbone, L. G., & Moncrief, V. 1976, ApJ, 207, 962
Forman, W., Churazov, E., Jones, C., et al. 2017, ApJ, 844, 122
Gottlieb, O., Lalakos, A., Bromberg, O., Liska, M., & Tchekhovskoy, A. 2022, MNRAS, 510, 4962
Jia, H., White, C. J., Quataert, E., & Ressler, S. M. 2022, MNRAS, 515, 1392
Kaaz, N., Antoni, A., & Ramirez-Ruiz, E. 2019, ApJ, 876, 142
Kaaz, N., Murguia-Berthier, A., Chatterjee, K., Liska, M., & Tchekhovskoy, A. 2022, arXiv:2201.11753
Kovalev, Y. Y., Pushkarev, A. B., Nokhrina, E. E., et al. 2020, MNRAS, 495, 3576
Lal, D. V., & Rao, A. P. 2007, MNRAS, 374, 1085
Leahy, J. P., & Williams, A. G. 1984, MNRAS, 210, 929
Li, J., Ostriker, J., & Sunyaev, R. 2013, ApJ, 767, 105
Li, Y., Gendron-Marsolais, M.-L., Zhuravleva, I., et al. 2020, ApJL, 889, L1
Liska, M., Hesp, C., Tchekhovskoy, A., et al. 2018, MNRAS, 474, L81
Liska, M., Chatterjee, K., Tchekhovskoy, A. E., et al. 2019, arXiv:1912.10192
Martizzi, D., Quataert, E., Faucher-Giguère, C.-A., & Fielding, D. 2019, MNRAS, 483, 2465
McKinney, J. C., Tchekhovskoy, A., & Blandford, R. D. 2013, Sci, 339, 49
Merritt, D., & Ekers, R. D. 2002, Sci, 297, 1310
Nakamura, M., & Asada, K. 2013, ApJ, 775, 118
Nemmen, R. 2019, ApJL, 880, L26
Nokhrina, E. E., Kovalev, Y. Y., & Pushkarev, A. B. 2020, MNRAS, 498, 2532
Palit, I., Janiuk, A., & Sukova, P. 2019, MNRAS, 487, 755
Parma, P., Ekers, R., & Fanti, R. 1985, A&AS, 59, 511
Porth, O., Chatterjee, K., Narayan, R., et al. 2019, ApJS, 243, 26
Prieto, M., Fernández-Ontiveros, J., Markoff, S., Espada, D., & González-Martín, O. 2016, MNRAS, 457, 3801
Proga, D., & Begelman, M. C. 2003a, ApJ, 582, 69
Proga, D., & Begelman, M. C. 2003b, ApJ, 592, 767
Ressler, S. M., Quataert, E., White, C. J., & Blaes, O. 2021, MNRAS, 504, 6076
Ressler, S. M., White, C. J., Quataert, E., & Stone, J. M. 2020, ApJL, 896, L6
Roberts, D. H., Saripalli, L., & Subrahmanyan, R. 2015, ApJL, 810, L6
Russell, H. R., Fabian, A. C., McNamara, B. R., & Broderick, A. E. 2015, MNRAS, 451, 588
Shapiro, S. L., & Teukolsky, S. A. 1986, in Black Holes, White Dwarfs and Neutron Stars: The Physics of Compact Objects, ed. S. L. Stuart & S. A. Teukolsky (New York: Wiley), 672
Stanzione, Dan, West, John, Evans, R. Todd, et al. 2020, in Frontera: The Evolution of Leadership Computing at the National Science Foundation (New York: Association for Computing Machinery)
Stawarz, Ł., Aharonian, F., Kataoka, J., et al. 2006, MNRAS, 370, 981
Suková, P., Charzyński, S., & Janiuk, A. 2017, MNRAS, 472, 4327
Suková, P., & Janiuk, A. 2015, MNRAS, 447, 1565
Tchekhovskoy, A., & Bromberg, O. 2016, MNRAS, 461, L46
Tchekhovskoy, A., Narayan, R., & McKinney, J. C. 2011, MNRAS, 418, L79
Ubertosi, F., Gitti, M., Brighenti, F., et al. 2021, ApJL, 923, L25
Waters, T., Aykutalp, A., Proga, D., et al. 2020, MNRAS, 491, L76
Xu, W., & Stone, J. M. 2019, MNRAS, 488, 5162
Yang, X., Joshi, R., Gopal-Krishna, et al. 2019, ApJS, 245, 17
Yuan, F., Wu, M., & Bu, D. 2012, ApJ, 761, 129
Zhuravleva, I., Churazov, E., Arévalo, P., et al. 2016, MNRAS, 458, 2902